C. R. Mecanique 341 (2013) 110–120

Contents lists available at SciVerse ScienceDirect

Comptes Rendus Mecanique

www.sciencedirect.com

Combustion, flow and spray dynamics for aerospace propulsion

Responses of V-flames placed in an HF transverse acoustic field from a velocity to pressure antinode

Florian Lespinasse [a,*], Françoise Baillot [a], Toufik Boushaki [b]

[a] CORIA UMR 6614 CNRS, site universitaire du Madrillet, 76801 Saint-Etienne-du-Rouvray, France
[b] ICARE UPR 3021 CNRS, 1C, avenue de la recherche scientifique, 45071 Orleans, France

ARTICLE INFO

Article history:
Available online 10 January 2013

Keywords:
Laminar combustion
Premixed flame dynamics
Acoustic azimuthal wave
Flame and flow instabilities

ABSTRACT

A V-flame stabilized by a vertical cylindrical rod in an annular jet is positioned at different points of an acoustic transverse field. Original mechanisms highlight flame and flow dynamics: vertical mass flow rate modulation resulting from a longitudinal-type wave induced by the pressure fluctuations of the transverse wave; jet and flame dissymmetry caused by acoustic energy effects; CH* emission modulations, related to heat release rate modulations, fluctuating at f_0, the forcing frequency, or at $f_0/2$ due to a vortex pairing phenomenon; flame blowout induced by the competition between vertical and lateral displacements due to the induced axial and transverse acoustic velocities, respectively.

Published by Elsevier Masson SAS on behalf of Académie des sciences.

1. Introduction

Increasingly stringent regulations imposed on combustion engines, especially gas turbines, lead to new technological choices and more complex chamber designs. Unfortunately, these changes have resulted in the development of combustion instabilities inside combustors [1,2]. In annular combustion chambers, instabilities often take the form of standing and traveling azimuthal modes which may be the most harmful not only for combustion efficiency, but also for the whole structural safety when the coupling of heat release fluctuations and resonant acoustics in the chamber is achieved. These dramatic consequences have resolutely led the combustion community to reinforce its efforts first to understand the physical mechanisms at the base of the triggering and development of these thermo-acoustic instabilities, second to control them. An increasing number of theoretical and numerical (see for example [3,4]) works have been devoted to the subject while some experimental studies are now in progress. Most of them concern turbulent swirled lean premixed flames in order to stick to industrial exigences, for example as done by Hauser et al. [5] and O'Connor et al. [6,7]. In [5] the authors placed the burner swirler at a velocity antinode of a low frequency transverse resonant mode (110–150 Hz). Longitudinal excitations could be also generated upstream of the swirler and superimposed to the transverse excitations. A spatial asymmetric distribution of high OH* emission intensity was found to rotate at the forcing frequency with an amplitude dependent on the transverse velocity amplitude. The transverse excitation induced a lateral oscillating displacement of the whole front on which a vertical one could be superposed due to imposed longitudinal excitations. O'Connor et al. [6,7] studied an annular flow behavior at a pressure or a velocity antinodes of a high frequency transverse acoustic field (0.4–1.2 kHz). In both cases, they highlighted a mass flow rate fluctuating across the burner exit at the forcing frequency, as observed in rocket engines where thermo-acoustic instabilities developed [8]. Inner and outer shear layers of the annular flow showed vortices located on both sides of the burner axis were in phase (out of phase) at a pressure (velocity) antinode. At a velocity antinode, longitudinal convective disturbances were superimposed on transverse acoustic disturbances, generating fluid instabilities from

* Corresponding author.
E-mail address: florian.lespinasse@coria.fr (F. Lespinasse).

1631-0721/$ – see front matter Published by Elsevier Masson SAS on behalf of Académie des sciences.
http://dx.doi.org/10.1016/j.crme.2012.10.015

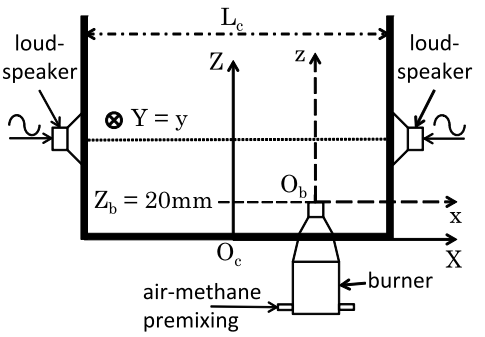

Fig. 1. Sketch of the set-up. (O_c, X, Y, Z) coordinate system attached to the bottom plate with O_c its center (solid line); (O_b, x, y, z) coordinate system attached to the burner (dashed line) with O_b the center of the exit section ($X_b = X, Y_b = 0, Z_b = 20$ mm); acoustic axis at $Z = 92$ mm (dotted line).

the burner exit sensitive to both longitudinal and transverse flow perturbations. The axial velocity fluctuations dominated in the shear layers, while transverse ones dominated in the jet core. Downstream, only transverse velocity fluctuations were observed. However, simultaneous complex phenomena lead to difficulty in interpreting fundamental mechanisms or even in hiding some of them. The need to perform laboratory studies is then crucial to highlight basic physical mechanisms driven by azimuthal modes and their coupling with flames, and finally to quantify involved quantities in order to control processes. In such a context, we have designed a set-up which allows the quantification of laminar V-flame dynamics to transverse acoustic excitations. In the following, the flame and jet characterization is first reported without acoustics. The acoustic response of the burner is determined. The high-frequency (0.5–1 kHz) acoustic standing pressure field is finely characterized without combustion. The fluidic system is described by means of time resolved optical diagnostics and image processing treatments specifically developed. Specific physical jet and flame features have been identified and quantified such as: spatially averaged axial velocities, jet exit areas, filaments and vortex arrays of the outer and inner layers, phase-averaged median curves of the flame front. Through their quantifications, original physical quantities and the mechanisms in which they are involved have been highlighted, in particular: vertical mass flow rate modulation resulting from a longitudinal-type wave induced by the acoustic pressure fluctuations, dissymmetric response of both the jet and flame caused by the product between the pressure and its gradient along the acoustic axis interpreted as the gradient component of the potential acoustic energy along this axis, CH^* emission, related to the heat release rate, fluctuating at the forcing frequency or at its first subharmonic according to a pairing phenomenon, flame blowout related to an oscillating movement of the front depending on the balance between a vertical and lateral displacements due to an induced longitudinal-type wave and the transverse wave respectively.

2. Experimental set-up and diagnostics

The experimental set-up, presented in Fig. 1, comprises a cylindrical burner, vertically fixed at the bottom of a steel semi-open acoustic cavity. Two driver units, facing each other, are embedded in the two opposite vertical walls of the cavity such that their common acoustic axis which passes through their centers is located at 92 mm from its bottom. They are characterized by a wide frequency range (0.5–20 kHz). They are supplied by a Hewlett Packard 8904 synthesizer and an Alesis RA500 amplifier. The vertical plates can slide on rails to vary the distance, L_c between them. For a given frequency, L_c is adjusted to ensure resonance of the acoustic pressure field produced by the loudspeakers. A high-intensity transverse mode is then created inside the cavity. Once L_c is fixed, the plates, maintained by two thin bars, can easily slide together. This allows the burner to be placed at any position inside the acoustic field. Flames issue from the premixing of methane and air flows whose mass flow rates are separately measured by Teledyne Hastings flow-meters.

2.1. The burner

The burner is composed of an upstream tube, 135 mm long with a 65 mm internal diameter, a converging profiled unit 59 mm long with an internal diameter reducing from 65 to 22 mm, and finally a convergent nozzle with a 10 mm exit diameter, D. A central rod is introduced inside the burner and aligned with its axis. The rod diameter, d_r is 3 mm. Its extremity stands out by $l_r = 3.5$ mm above the burner exit.

The burner response to an external acoustic sine wave excitation has been determined without any flow in a free air. It has been explored in the range 10–1100 Hz. The results, cited in [9], show the burner behaves like a Helmholtz resonator with a peak $f_H \approx 130$ Hz, except around 1 kHz where a secondary peak is measured and interpreted as the signature of a 3/4 wave mode of an equivalent round tube.

2.2. Diagnostics

Several diagnostics are used to analyze how the flame and the flow respond to a transverse wave.

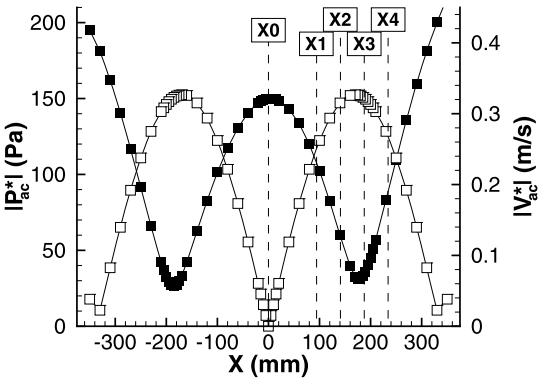

Fig. 2. Acoustic field vs. X for 510 Hz, $k_Y = 0.68$ m^{-1} and $k_Z = 2$ m^{-1}: filled symbol: experimental pressure amplitude $|P^*_{ac}|(X, Y = 0, Z = 30$ mm$)$; open symbol: velocity amplitude calculated from Eq. (1) and $V_a = (P_a k_X)/(2\pi\rho f_0)$; $(\mathrm{Xi})_{1\leqslant i\leqslant 5}$: burner positions.

2.2.1. For the jet

All measurements are made with the flame. Vertical and radial velocities, $U(\vec{x}, t)$ and $V(\vec{x}, t)$, are measured by a Laser Doppler Velocimeter (LDV) system composed of a 4 W argon ion laser as the luminous source, a TSI system using a fiber optic probe and an IFA 755 processor. Olive oil particles with a 1 μm mean diameter d_p are seeded in the cold premixed flow to be used as the scattering particles. Considering the size of the set-up, measurements are made from 3 mm above the burner exit so that a measurement domain is small enough to ensure a good resolution in space. The Stokes number of an oil particle, S_k, defined as the ratio of its response time, τ_p, over the acoustic time, τ_{ac}. $S_k = \tau_p/\tau_{ac} = \frac{\rho_p d_p^2 f_0}{18\mu}$ is lower than 3×10^{-3} in the frequency range chosen here (510–1010 Hz). So flow dynamics is well described by oil droplet displacements. Moreover, the sampling rate is higher than 20 000 validated data per second; on average, 40–50 (20–25) data per cycle are validated for each velocity channel at 510 Hz (1010 Hz). Thus, regarding acoustic time scales, time-resolved measurements of unsteady velocities are obtained.

A 2D scattering technique is used to visualize the gas flow structure by lighting the premixed jet seeded with oil droplets by means of vertical or horizontal laser sheets whose luminous source is a continuum laser CNI MGL-W532 of 1.2 W. Vertical sheets contain both acoustic and burner axes. Horizontal sheets are positioned at a distance from the burner exit of 1 or 5 mm. Views are recorded by a high-speed digital camera Phantom V12.1, operating at 7920 images/s (1024 × 768 pixels, 12 bit). A 180 mm Nikon AF Nikkor lens ($f/2.8$) gives a 0.034 mm/pixel image resolution.

2.2.2. For the flame

The spatial flame evolution is qualified over time in horizontal or vertical laser sheets by following the isotherm of evaporation of oil droplets, separating the luminous domain of the incoming seeded jet from the black domain of hot gases free from droplets, by means of the camera Phantom V12.1. 1000 images per series are recorded at 7920 images/s. In some cases, they have been used to reconstruct a phase-averaged flame evolution based on 7 phases distributed over one period. To characterize the front behavior, the flame emission is captured by an intensified CCD Princeton Instrument camera (5 images/s, 576 × 384 pixels, 14 bit) simultaneously to vertical laser tomography cuts of the seeded jet. A 105 mm UV Nikkor lens ($f/5.6$) fitted on the camera leads to a resolution of 0.069 mm/pixel. The global flame dynamics is finally quantified by its overall CH* emission recorded by a photomultiplier Hamamatsu H6779 (PM) equipped with an interferential filter centered at $\lambda = 430$ nm with a Full Width at Half Maximum = 10 nm (±2 nm). The PM is positioned at 40 cm away from the flame in order to collect all the CH*-light emitted by the flame and to be outside the acoustic cavity.

Two microphones *B*&*K* 4182 model with a 1 Hz–20 kHz frequency response register pressure fluctuations. They can be placed all together in the acoustic cavity near the flame along the acoustic axis, but also one in the cavity and the other one in the burner bottom.

Imaging, pressure and CH* emission fluctuations have been simultaneously measured.

3. Acoustic pressure field without a flame

The position of a point in the cavity is specified by means of the Cartesian coordinate system (O_c, X, Y, Z) where O_c is the center of the horizontal bottom plate, (O_c, X) is the horizontal axis perpendicular to the vertical plates and (O_c, Z) is the ascending vertical axis (see Fig. 1). Here, the loudspeakers are chosen to work in phase and their power supplies are adjusted to deliver the same pressure amplitude in the cavity center. The resulting pressure amplitude measured along an X-axis parallel to the acoustic axis, shows an antinode at $X = 0$ and two minima near $X = \pm L_c/4$. An example of such a profile measured along the X-axis is given in Fig. 2 for the forcing frequency $f_0 = 510$ Hz and $L_c = 75$ cm.

The harmonic cavity modes are found to be negligible. Both residual traveling waves and slight harmonic modes may explain pressure amplitude is not quite null at the nodes. So the pressure fluctuations $P_{ac}(X, Y, Z, t)$ may be expressed

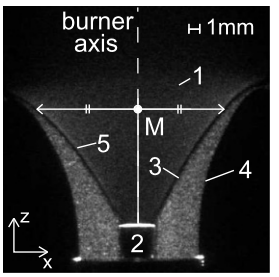

Fig. 3. Vertical laser tomography views of the seeded jet without acoustics; 1: direct flame emission; 2: stabilization rod; 3: inner shear layer; 4: outer shear layer; 5: isotherm of evaporation of oil droplets; M: middle point defining a curve (C_0) of Fig. 5.

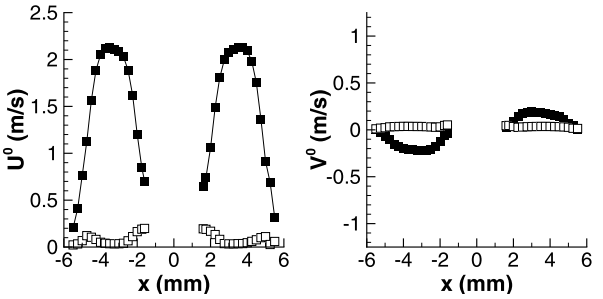

Fig. 4. Mean (filled symbol) and rms (open symbol) velocity profiles without acoustics for $U_{bulk} = 2.1$ m/s at $z = 4$ mm; (a) vertical component U^0; (b) horizontal component V^0.

as a sine wave function of time: $P^*_{ac}(X, Y, Z)\cos(2\pi f_0 t)$. Measurements of the pressure amplitudes $|P^*_{ac}|(X, Y, Z)$ according to X, Y and Z show that they are well approached in the domain $-L_c/4 \leqslant X \leqslant L_c/4$ by $P^*_{ac}(X, Y, Z) = P_a \cos(k_X X)\cos(k_Y Y)\cos(k_Z Z)$ with $k_X = (2\pi)/L_c$. Let us note that for $|X| \geqslant L_c/4$, the walls equipped with loudspeakers impose a matching condition to the pressure field whose amplitude is higher than the theoretical solution. This also contributes to a non null pressure rms amplitude at the minimum since the instantaneous position of that minimum may slightly deviate from the theoretical pressure node position ($L_c/4$) by ±4%. However a calculation with COMSOL shows the transverse standing wave assumption is well-satisfied. The variation of the pressure amplitude with coordinates (Y, Z) in a domain occupied by the flame (-30 mm $\leqslant Y \leqslant 30$ mm, $0 \leqslant Z \leqslant 70$ mm) is at the most about 1.0%. Finally, the acoustic field can be interpreted as a planar standing wave in the X-direction corresponding to the second transverse mode of the cavity (see also [10]). The associated acoustic velocity field in the cavity, $\overrightarrow{V_{ac}}(X, Y, Z, t)$, may be then approached by Eq. (1):

$$\overrightarrow{V_{ac}}(X, Y, Z, t) = -\frac{1}{\rho}\int \overrightarrow{grad}(P_{ac})\,\mathrm{d}t \cong V_a \sin(k_X X)\cos(k_Y Y)\cos(k_Z Z)\sin(2\pi f_0 t)\vec{e}_x \tag{1}$$

with $V_a = (P_a k_X)/(2\pi\rho f_0)$ since the two other components V_{ac_Y} and V_{ac_Z} are negligible in the whole investigation domain. An example of the acoustic velocity amplitude profile along the X-axis for $Y = 0$ and $Z = 30$ mm, calculated from the measured acoustic field, is given in Fig. 2. As determined experimentally, if the pressure minimum is not an exact pressure node, it is an effective acoustic velocity antinode where some residual pressure fluctuations persist. The center of the burner exit section, O_b, is positioned at $(X_b, Y_b = 0, Z_b = 20$ mm). Finally, in the following, positions of a measured quantity are specified from the burner exit plane by the coordinate system $(O_b, x = X - X_b, y = Y, z = Z - Z_b)$. Pressure fluctuations P_{ac} measured close to the pressure antinode at point $(X = 10$ mm, $Y = 10$ mm, $Z = Z_b + 10$ mm) are used as the reference parameter of the acoustic field. Their amplitude is noted P_{ref} afterwards. According to the previous remarks, five positions, labeled $(\mathrm{Xi})_{0 \leqslant i \leqslant 4}$ in Fig. 2, are chosen to place the burner: (0) X0 = 0 (pressure antinode), (1) X1 = $L_c/8$ (acoustic intensity antinode where the acoustic flux $P_{ac}V_{ac}$ is maximum), (2) X2 = $3/16L_c$, (3) X3 = $L_c/4$ (near the velocity antinode), (4) X4 = $5/16L_c$.

4. Flame and jet without acoustics

Several bulk velocities, U_{bulk} at rich, stoichiometric and lean equivalence ratios, φ were examined. Results are presented here for $U_{bulk} = 2.1$ m/s and $\varphi = 1$. Fig. 3 shows a typical instantaneous view of the direct V-flame emission and vertical laser tomography of the seeded jet. Fig. 4 reports representative radial profiles of the mean velocity components (U^0_{mean}, V^0_{mean}) and rms velocity components (U^0_{rms}, V^0_{rms}) measured at $z = 4$ mm, just above the rod extremity.

Vertical and radial velocity profiles result from the annular flow due to the rod. The absence of data in the mid-zone is due to the oil droplet evaporation caused by the flame. The flow is laminar, with a very weak residual fluctuating part

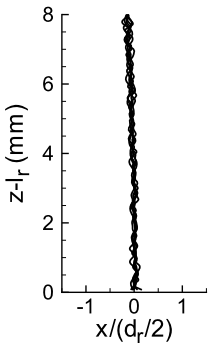

Fig. 5. 7 positions of the flame median curve (C_0) without acoustics.

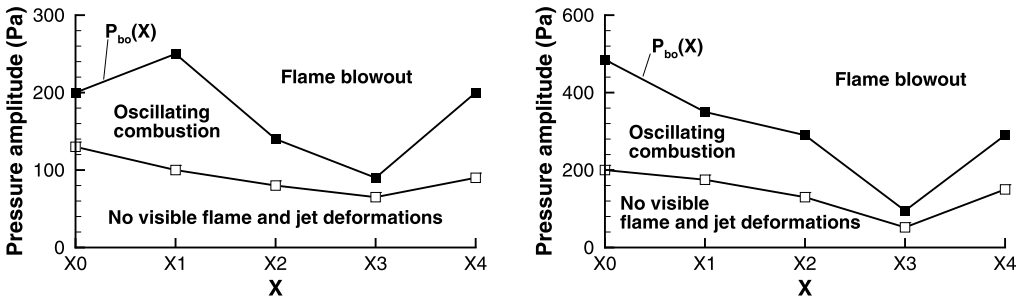

(a) f_0=506Hz (b) f_0=1012Hz

Fig. 6. Operating conditions in terms of local pressure amplitude vs. position Xi in the transverse acoustic field: filled squares: flame blowout limit $P_{bo}(X)$; open squares: lower limit underneath no visible flame and jet deformations are noted.

(U^0_{rms}/U^0_{mean}, V^0_{rms}/V^0_{mean} are smaller than 3%). No vortices are present, neither in the outer shear layer separating the premixed jet and the surrounding air, nor in the inner shear layer due to the rod. It is similar to what was observed by [11]. Moreover, the V^0_{mean}-shape indicates streamlines are deviated outwards from the vertical direction by the presence of the flame.

Flame adaptation to the flow is described via several quantities. Its spatial occupancy is characterized by the median curves (C_0), obtained from several instantaneous vertical time-resolved laser tomography images. They are constituted of the middle points M of horizontal segments located between the two parts of the isotherm of evaporation of oil droplets (e.g. in Fig. 3). (C_0) give information about the flame symmetry. Fig. 5 reveals the flame stays symmetric without acoustics.

Secondly, the global flame dynamics is characterized by CH* emission which is characteristic of the heat release rate in the present lean or stoichiometric conditions [12].

5. Results

The burner, marked by its axial coordinate X_b, is placed successively at one of the five positions Xi defined in Section 3 ($X_b = \mathrm{Xi}$). The local pressure amplitude at the burner exit $P_{X_b} = |P^*_{ac}|$ ($X = \mathrm{Xi} + 10$ mm, $Y = 10$ mm, $Z = Z_b + 10$ mm) is fixed between a lower limit where no visible flame and jet deformations are noted, and the flame blowout limit, $P_{bo}(X) = |P^*_{ac}|$ ($X, Y = 10$ mm, $Z = Z_b + 10$ mm) (see Fig. 6).

The local deformation of the jet is qualified by the vortical structures emitted from the burner exit or formed downstream during flow convection. Their displacements recorded by the high-speed camera are well time-resolved. The global seeded jet deformation is quantified at the burner exit ($z = 1$ mm) by laser-lightened pixel areas of two complementary horizontal surfaces, A_V and A_P, recorded by the high-speed camera (see Fig. 7). The surfaces are enclosed in a domain $\mathscr{D}$ coincident with the nozzle cross-section and are separated by a line normal to the acoustic axis cutting $\mathscr{D}$ in two equal parts, $\mathscr{D}_{1/2}$ of area $A_{\mathscr{D}_{1/2}} = \pi D^2/8$. A_V is the surface nearer to a velocity antinode and A_P to a pressure antinode. Their areas, also called A_V and A_P for brevity, are calculated by summing pixels whose gray levels are higher than the ground noise and reduced by $A_{\mathscr{D}_{1/2}}$. This description is completed by the spatially averaged axial velocities of the seeded jet, $\overline{U}_{right}(t)$ and $\overline{U}_{left}(t)$, as proposed by [6], determined by LDV at $z = 4$ mm along half the annular diameter ($d_r/2 < |x| < D/2$) for the right and left sides of the burner respectively. All the quantities have been correlated to the pressure signals simultaneously recorded near the flame at point ($x = 10$ mm, $y = 10$ mm, $z = 10$ mm).

Tomography views of the seeded jet in the presence of the flame are shown in Figs. 8 and 9. They are put in the same spatial arrangement as that with which measurements have been made along the X-axis.

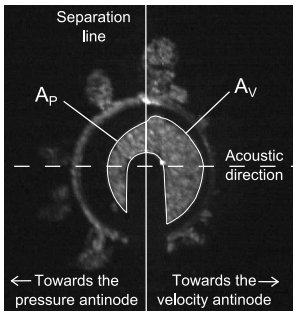

Fig. 7. Laser tomography horizontal cut at $z = 1$ mm with areas A_V and A_P at X1 for $P_{X_b} = 250$ Pa and $f_0 = 510$ Hz.

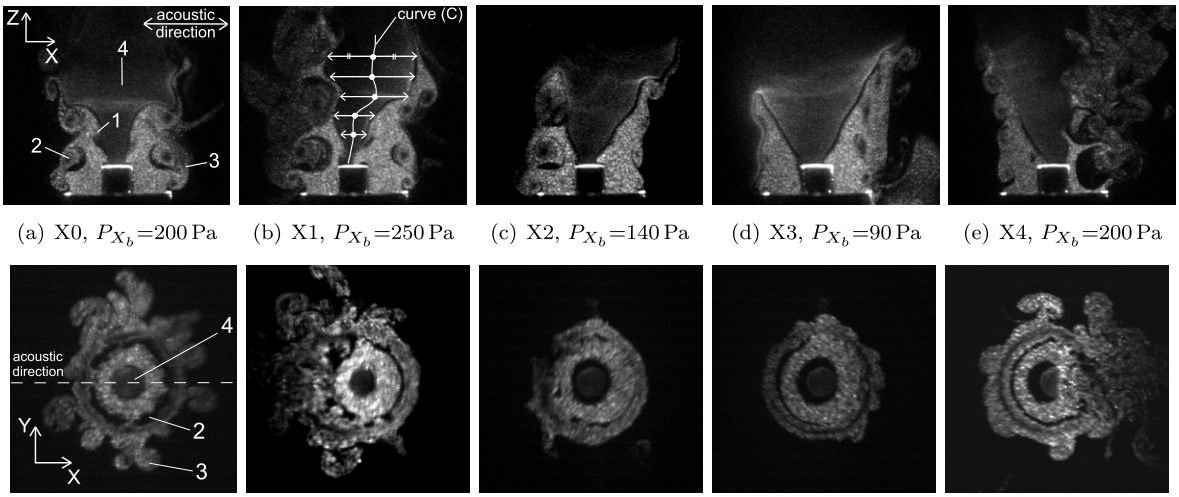

(a) X0, P_{X_b}=200 Pa (b) X1, P_{X_b}=250 Pa (c) X2, P_{X_b}=140 Pa (d) X3, P_{X_b}=90 Pa (e) X4, P_{X_b}=200 Pa

(f) X0, P_{X_b}=200 Pa (g) X1, P_{X_b}=250 Pa (h) X2, P_{X_b}=140 Pa (i) X3, P_{X_b}=90 Pa (j) X4, P_{X_b}=200 Pa

Fig. 8. Laser tomography views of the seeded jet at Xi in the transverse acoustic field for $f_0 = 506$ Hz and $P_{X_b} = P_{bo}$(Xi) (blowout limit of Fig. 6): (a)–(e) vertical cuts; (f)–(j) horizontal cuts at $z = 5$ mm. 1: vortex created in the inner shear layer; 2: vortex created in the outer shear layer; 3: filament; 4: direct flame emission. View 8(b) shows how curve (C) is determined.

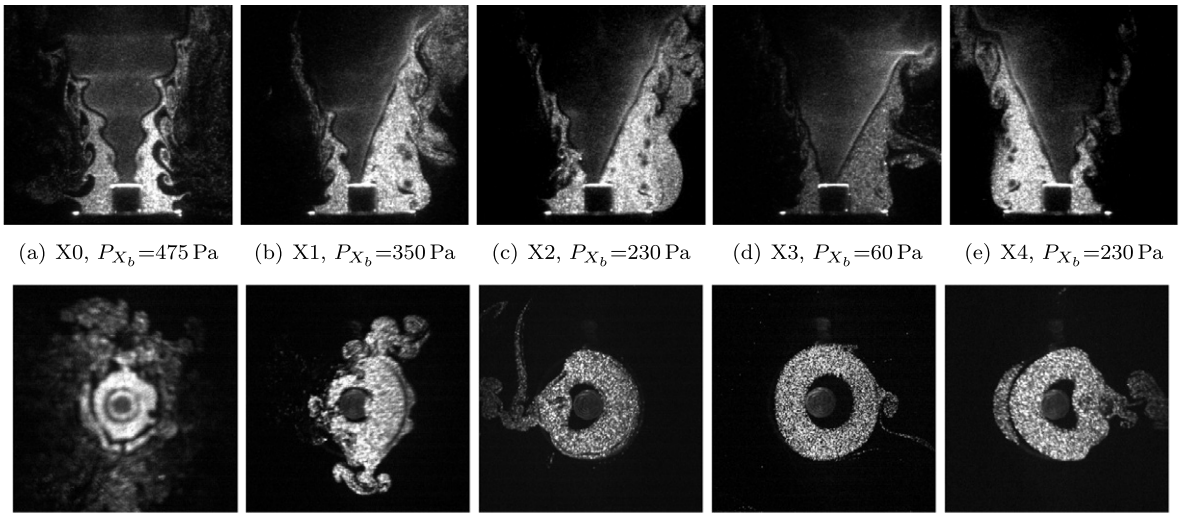

(a) X0, P_{X_b}=475 Pa (b) X1, P_{X_b}=350 Pa (c) X2, P_{X_b}=230 Pa (d) X3, P_{X_b}=60 Pa (e) X4, P_{X_b}=230 Pa

(f) X0, P_{X_b}=475 Pa (g) X1, P_{X_b}=350 Pa (h) X2, P_{X_b}=230 Pa (i) X3, P_{X_b}=60 Pa (j) X4, P_{X_b}=230 Pa

Fig. 9. Laser tomography views of the seeded jet at Xi in the transverse acoustic field for $f_0 = 1012$ Hz and $P_{ref} = 475$ Pa: (a)–(e) vertical cuts; (f)–(j) horizontal cuts at $z = 5$ mm.

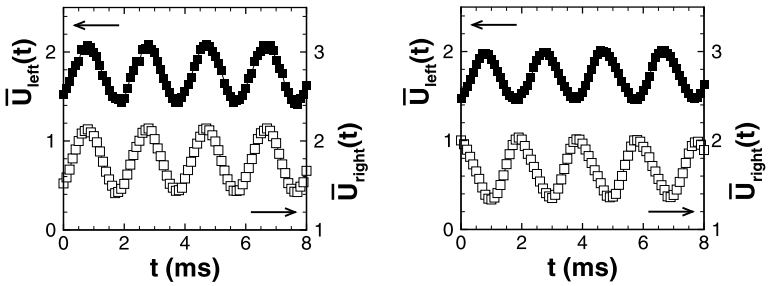

(a) X0, P_{X_b}=145 Pa (b) X3, P_{X_b}=70 Pa

Fig. 10. Spatially averaged axial velocities along half the annular length on the right (filled symbol) and left (open symbol) sides of the burner at $z = 4$ mm for $f_0 = 510$ Hz and $U_{bulk} = 1.6$ m/s.

5.1. Periodic modulation of the mass flow rate

One dominant effect of the transverse wave is to modulate the mass flow rate at f_0 through the burner exit as observed by [6,8,10]. This fluctuation is quantified by the temporal signals of $\overline{U}_{right}(t)$ and $\overline{U}_{left}(t)$. They are modulated in phase as shown in Fig. 10 provided that the burner is not located in the velocity antinode vicinity. Indeed, as the theoretical pressure node is a singular location for pressure fluctuations which undergo a phase jump of π, this may result in an out-of-phase evolution of the spatially averaged velocities between the right and left sides of the burner (e.g. in Fig. 10(b)). Since the pressure node becomes less noticeable as the pressure amplitude increases, this phase jump tends to disappear. The very weak pressure fluctuations at the burner bottom indicate that no active amplification could be induced by the burner. This is consistent with the nonexistent acoustic burner response at these frequencies. Around 1000 Hz, pressure fluctuations are much less attenuated, suggesting that the burner could contribute to amplify the mass flow rate modulation. Nevertheless, observations at the velocity antinode confirm the burner is mainly passively involved. To conclude, the transverse mode induces a vertical fluctuating motion resulting from a dominant vertical mass flow rate modulation with a weak possible supplementary contribution of a longitudinal resonant mode of the burner.

5.2. Flame and jet dynamics at the pressure antinode X0

For conditions just above the lower limit of Fig. 6, the overall jet evolution in space, described through A_V and A_P remains well symmetrical, but small reverse flows periodically enter inside the burner. They grow with the pressure amplitude. An illustration, given in Figs. 11(a) and 11(d) for pressures at the flame blowout limit, shows their presence via steep hollows, so intense that they contract the initial jet by 60% before being rapidly pushed out. By analyzing the jet, a periodic shedding of azimuthal vortices is shown to form from the burner exit in the outer boundary layer (see Figs. 8(a) and 8(f) and Figs. 9(a) and 9(f)). They are disturbed by several streamwise filaments ejected all around the jet circumference, which leads to large zones of reactive matter whose movement is decelerated by the surrounding air, even up to becoming more or less stagnant.

At the same time, as the pressure amplitude is increased, the inner layer becomes active and generates (small) vortices. Different vortex arrays may occur depending on the pressure level, the forcing frequency and the balance between the developments of the outer and inner layers. In such a context, the flame adopts periodic responses, showing different types of wrinkling directly linked to the development of the above-mentioned vortex arrays. Here, two examples are given: at 510 Hz Figs. 8(a) and 8(f) show a flame front wrinkling piloted by the outer layer; at 1010 Hz Figs. 9(a) and 9(f) show a wrinkling piloted by the inner layer. A detailed analysis can be found in [9]. The flame front evolves symmetrically to the burner axis. The flame impact in horizontal planes remains well circular (see Figs. 9 and 8). From a direct flame emission image processing, the flame foot is verified to periodically move up and down above the rod, the vertical displacement amplitude increasing with P_{ref} increase.

As the flame dynamics is locally determined by its wrinkling, it can be globally quantified by means of the whole CH* emission, related to the flame surface area variation. PSD of the CH* emission intensity signal, $I_{CH^*}(t)$ (reduced by the mean intensity $I^0_{CH^*}$) indicate the flame responds at the forcing frequency f_0 (e.g. in Fig. 12(a)). For sufficiently high pressure amplitudes, the flame dynamics may be driven by the subharmonic mode $f_0/2$ (see Fig. 13(a)). This non-linear frequency bifurcation occurs when a pairing-type mechanism occurs in the outer layer for which, however, no merging between the involved vortices is achieved before they impact the front, as introduced in [9]. Finally, the acoustic pressure through its amplitude and frequency drives both jet dynamics (relative action of the two layers, vortex strength and size, ...) and flame dynamics (symmetric shapes and wrinklings, area variations and CH* fluctuations).

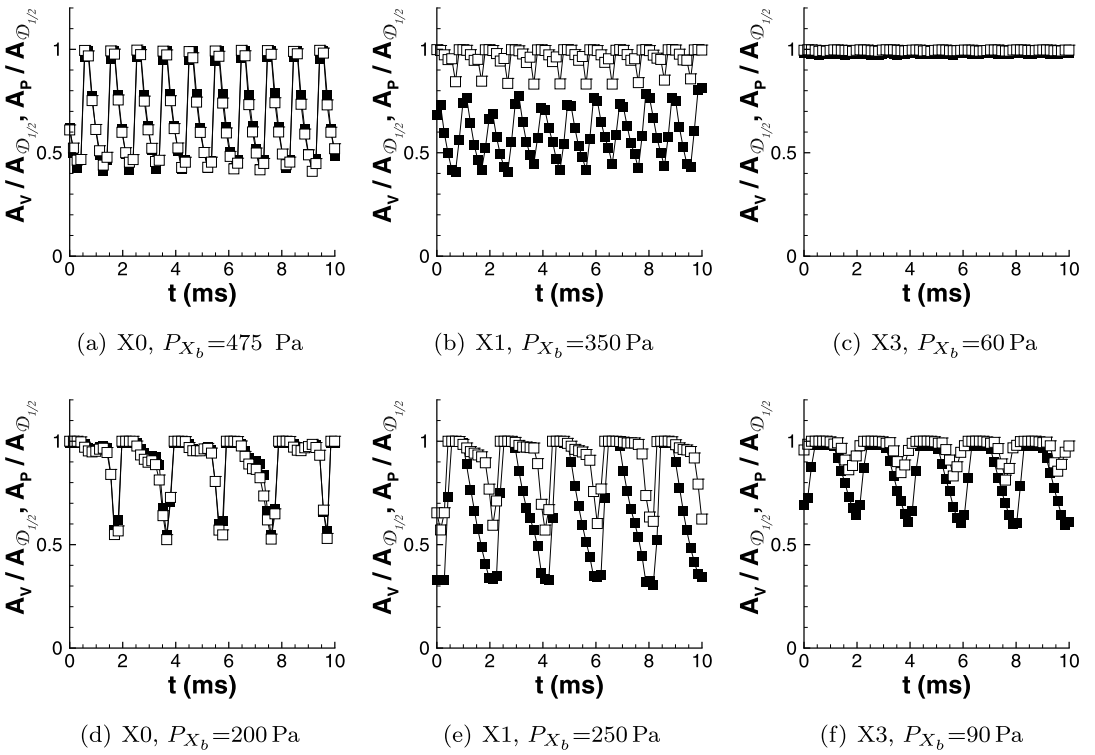

(a) X0, P_{X_b}=475 Pa (b) X1, P_{X_b}=350 Pa (c) X3, P_{X_b}=60 Pa

(d) X0, P_{X_b}=200 Pa (e) X1, P_{X_b}=250 Pa (f) X3, P_{X_b}=90 Pa

Fig. 11. Reduced areas $A_V/A_{\mathscr{D}_{1/2}}$ (open symbol) and $A_P/A_{\mathscr{D}_{1/2}}$ (filled symbol) at $z = 1$ mm vs. time: (a)–(c) for 1012 Hz and $P_{ref} = P_{bo}(\mathrm{X0}) = 475$ Pa; (d)–(f) for 506 Hz and $P_{X_b} = P_{bo}(\mathrm{Xi})$ (see Fig. 6).

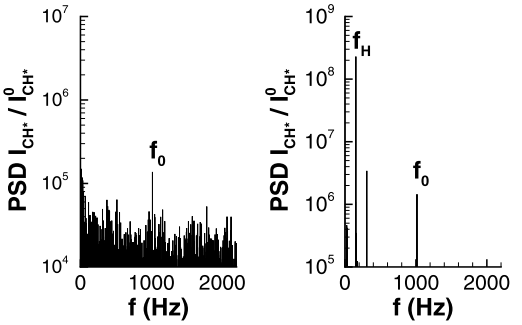

(a) X0, P_{X_b}=475 Pa (b) X3, P_{X_b}=60 Pa

Fig. 12. PSD of no-filtered CH* emission signals at 1012 Hz $P_{ref} = P_{bo}(\mathrm{X0}) = 475$ Pa.

5.3. Asymmetrical responses of the reactive fluidic system located at positions Xi different from X0

Whatever the positions $(\mathrm{Xi})_{1\leqslant i\leqslant 4}$, the flame symmetry and that of the jet related to the axial plane (Π_{Xi}) normal to the acoustic direction, are broken. This can be seen in Fig. 8 at 506 Hz and Fig. 9 at 1012 Hz: not only the size of left and right vortices greatly differs, but also the filaments production. Outer vortices located on the side nearer to a pressure antinode are bigger than the vortices located on the other side (see Fig. 9). This dissymmetry, highlighted by the previous local flow features, is also quantified by the global quantities A_V and A_P, except when the pressure level is not high enough to produce reverse flows (e.g. Fig. 11(c)). A_V, located nearer to the velocity antinode, is much less deviated from the unperturbed area comparatively to A_P, located nearer to the pressure antinode, for which the reverse flows action appears to be emphasized in amplitude and in duration (see Fig. 11). Contrary to A_V, domain A_P may never coincide with $\mathscr{D}_{1/2}$ since the reduced area $A_P/A_{\mathscr{D}_{1/2}}$ does not reach 1 (e.g. in Fig. 11(b), $0.45 \leqslant A_P/A_{\mathscr{D}_{1/2}} \leqslant 0.75$). A_P is always tightened by the incoming and outgoing flows of the unseeded air during the periodic evolution. The half-jet associated to A_P issues from the part of the internal flow, presenting an oscillating layer separation at the wall inside the burner at all times.

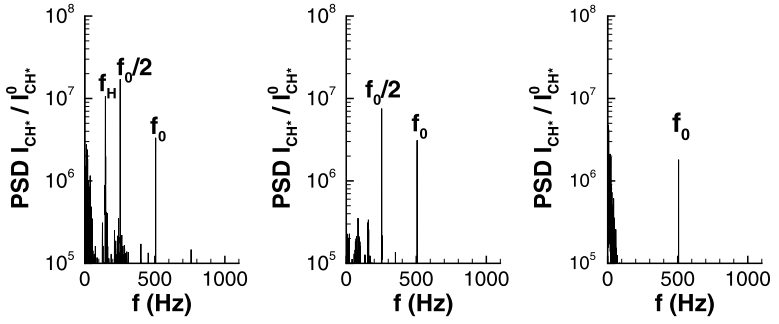

(a) X0, P_{X_b}=200 Pa (b) X1, P_{X_b}=250 Pa (c) X3, P_{X_b}=90 Pa

Fig. 13. PSD of no-filtered CH* emission signals at 506 Hz for $P_{X_b} = P_{bo}$(Xi) (see Fig. 6).

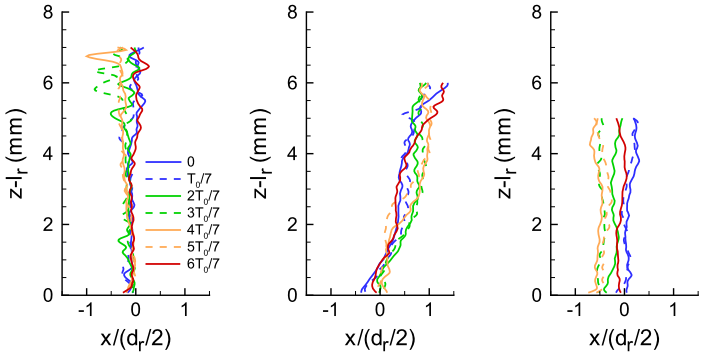

(a) X0, P_{X_b}=200 Pa (b) X1, P_{X_b}=250 Pa (c) X3, P_{X_b}=90 Pa

Fig. 14. Median curves (C) of the flame in the axial plane (O_b, x, z) obtained from phase-averaged series of 1000 images classified according to 7 equitemporal phases for $f_0 = 506$ Hz and $P_{X_b} = P_{bo}$(Xi) at positions X0, X1 and X3 (l_r: distance of the rod extremity to the burner exit; d_r: rod diameter).

The jet dissymmetry at positions X1 to X4 generates flame dissymmetry: the half-fronts, left and right in the vertical views, are no more identical, and the flame impact, visualized in horizontal views in Figs. 8 and 9(g)–(j) by a dark zone, is no more circular nor centered at the burner axis. The vortical jet structure is able to greatly wrinkle the half-front located towards the nearer pressure antinode, but is practically inefficient to wrinkle the opposite half-front which is rather smooth (see Figs. 9 and 8(b)–(e)). Due to this dissymmetric vortex pattern, the front is tilted and the flame base is laterally displaced relative to the burner axis. These features are clearly quantified by seven phase-averaged median curves (C), which are deduced from series of 1000 images, as shown in Fig. 8(b). A representative illustration of curves (C) obtained at 510 Hz is given in Fig. 14. At X0, all curves (C) remain vertically superimposed at (or close to) $x = 0$ over time. At X1, X2 and X4, curves (C), and consequently the flame, are greatly inclined over time towards the nearer velocity antinode by an angle around 16° for 510 Hz and 13° for 1010 Hz (e.g. for X1 in Fig. 14(b)). This angle is smaller at 1010 Hz than 510 Hz due to a difference in the front shape which is imposed by the flame response type. Simultaneously a lateral shift along the x-axis indicates the flame foot is no more centered on the rod as shown in Figs. 14(b) and 14(c). Moreover, curves (C) superimposed at X0 are progressively not coincident when the burner is displaced towards the velocity antinode X3. In the basin of influence of the latter one (X3, X2 and X4), curves do not merge over time, indicating the flame front is submitted to a periodic displacement as a whole along the x-axis which is maximum at X3 (see Fig. 14(c)).

After analyzing the jet and flame responses quantified for every positions Xi, they are mutually compared for a given acoustic pressure field. Vertical and horizontal images reveal the transverse wave impact on both jet and flame aspects is less remarkable as the burner is moved from positions X0 to X3 whatever f_0: smaller and weaker vortices are formed as well in the outer layer as in the inner layer, and a decrease in the amplitude of the reverse flows which contract the jet is noted. An illustration is given in Fig. 9 for 1010 Hz. But this attenuation is more discernible on the burner side nearer the velocity antinode. (As expected, the jet deformation at position X4 is reversed relatively to plane (Π_{X4}) compared to that at position X2.) Moreover, the above-mentioned lateral displacement becomes dominant compared to the flame foot vertical oscillating movement which decreases from X0 to X3.

Finally, flame dynamics through the overall CH* emission integrates all these local deformations. It is modulated at f_0 (see Figs. 12(b) and 13(c)), or for sufficiently high pressure amplitudes, at $f_0/2$ (see Figs. 13(b)) when the pairing phenomenon is involved as explained Section 5.2.

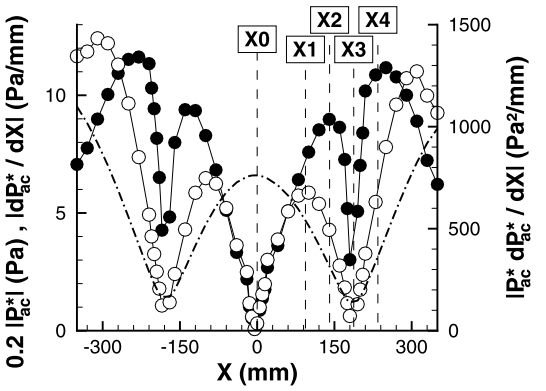

Fig. 15. Acoustic pressure X-gradient (•) and potential energy density e_{ac} X-gradient multiplied by ρc^2 (∘) vs. X at ($Y = 0, Z = 30$ mm) for 510 Hz determined from the pressure data $|P^*_{ac}|$ (— · —·) introduced in Fig. 2.

5.4. Driving physical quantities

5.4.1. Acoustic pressure amplitude

A direct action consecutive to the periodic bulk compression/dilation, is to vertically modulate the flow provided that the mean dynamic pressure of ejected gases is lower than the acoustic pressure amplitude in the cavity. This effect is similar to that one produced by a longitudinal excitation. Above a threshold (see Fig. 6), the acoustic pressure determines the whole jet vortical structure: filaments and vortices' arrays generated in both outer and inner layers, vortex size and strength which can lead to a pairing mechanism in the outer layer, jet contraction by reverse air flows, relative predominance of one layer over the other one, and finally vortex efficiency of each layer to wrinkle or wrap the flame front. As verified here, the shape type adopted by the flame at the pressure antinode is then kept at the other acoustic field positions. The flame surface, periodically modulated by jet vortices via large area variations, generates strong CH* emission fluctuations, leading to heat release rate fluctuations at the same frequency, f_0 or $f_0/2$ in the presence of a pairing phenomenon in the outer layer. Jointly, the flame foot is submitted to a vertical periodic displacement.

5.4.2. Transverse acoustic velocity amplitude

The acoustic velocity amplitude V_a (see theoretical expression in Section 3 and Eq. (1)) must attain an order of magnitude similar to the unperturbed jet velocity to compete with the initial flow impulsion (see [10]). It is achieved in the basin of influence of the velocity antinode. The effect on the flame is to laterally displace it periodically. CH* emission fluctuations at velocity antinode are smaller than at pressure antinode and result from residual fluctuating pressure effects.

5.4.3. Competition between acoustic pressure and transverse velocity on flame stabilization

For a sufficiently high pressure level, at the pressure antinode the flame which is periodically displaced in the vertical direction by longitudinal disturbances, is pushed at a downstream distance which avoids any possible stabilization and leads to its blowout. At the velocity antinode, the flame which is periodically displaced, but laterally this time by the transverse perturbations, is pushed as to stick out the stabilization rod, which also provokes its blowout. These two mechanisms compete to break flame stabilization according to opposite influences whatever positions in the acoustic direction: a lower vertical displacement is observed when the lateral displacement is increased. A similar feature was noted by [5] in another configuration.

5.4.4. Crossed contribution of pressure and pressure X-gradient

Symmetry rupture of both flame and jet morphologies is observed in the acoustic direction. This rupture is marked by a discrepancy in the vortex formation/development and flame shape (wrinkling and tilting) between the regions located on both sides of axial plane (Π_{Xi}) normal to the acoustic axis (left and right sides in views). The observed disturbances are always maximum on the side nearer to a pressure antinode. Acoustic velocity and pressure levels cannot explain it. Indeed, at the velocity antinode X3 where the transverse velocity amplitude is maximum, dissymmetry is almost nonexistent. On the contrary, the acoustic velocity amplitude is very small at location X1 but dissymmetry is the most visible. For its part, the pressure X-gradient (see in Fig. 15) can create dissymmetry: the symmetry is maintained where $\partial P^*_{ac}/\partial X$ is null at X0, the pressure antinode; the dissymmetry pattern is greatly discernible at X2 in the vicinity of $|\partial P^*_{ac}/\partial X|_{max}$. However, while $|\partial P^*_{ac}/\partial X|$ is smaller at X1 than at X2, dissymmetry is the most noteworthy at X1. If the presence of the X-gradient is a necessary condition to have dissymmetry, it is not sufficient to explain its intensity. To note an effective dissymmetry, a pressure amplitude high enough must also exist locally. Finally, $\partial P^*_{ac}/\partial X$ conditioned by P^*_{ac} can explain the way dissymmetry appears along the X-axis. The spatial variation of the product $|P^*_{ac}\partial P^*_{ac}/\partial X|$, shown in Fig. 15, well agrees with the spatial dissymmetry distribution as that ones of Figs. 8 and 9: null at X0 and X3 where P^*_{ac} $\partial P^*_{ac}/\partial X$ is null; maximum at X1 where $|P^*_{ac}\partial P^*_{ac}/\partial X|$ is maximum. So the dissymmetry feature spatially follows a periodic evolution of wave number $2k$.

5.4.5. Energetic interpretation of the dissymmetry

The previous results analysis suggests dissymmetry is induced not by pure dynamic (pressure only) or kinematic (velocity only) effects, but by energetic effects. These latter ones are characterized by the acoustic energy density $e_{ac} = e_{ac_p} + e_{ac_c}$ ($e_{ac_p} = P_{ac}^2/(2\rho c_s^2)$ the potential part and $e_{ac_c} = \rho V_{ac}^2/2$ the kinetic part) and the acoustic energy flux density $\overrightarrow{f_{ac}} = P_{ac}\overrightarrow{V_{ac}}$, linked by the linearized momentum equation. As the acoustic field is well approached by a stationary wave (see Section 3), these quantities are periodic with wave number $2k$. Jet dissymmetry is essentially produced in the near field by convective disturbances which generate flame dissymmetry. This implies potential acoustic effects might have greater impact on the fluidic system than kinetic effects, even though their order of magnitude are similar, since their intrinsic features are different.

6. Conclusion

This work reports new results of an original experiment describing the interaction between an acoustic transverse wave and a V-flame positioned at different points of the field. Several quantities responsible for flame and jet oscillations are identified. Pressure fluctuations inducing a longitudinal-type modulation impose flame area variations, front vertical displacement and CH^* emission fluctuations, which may lead to thermo-acoustic coupling between transverse wave and combustion as observed in industrial engines. On the other hand, velocity fluctuations produce lateral whole-flame oscillations. These two effects compete together and in particular for blowing out the flame in the presence of high pressure levels. Energy effects are highlighted to be responsible for jet and, consequently, flame dissymmetry. Pressure measurement seems to be insufficient to quantify thermo-acoustic coupling and flame extinction. Acoustic velocity and pressure gradient characterization is also necessary to understand the fluidic system response.

References

[1] F.E.C. Culick, Unsteady motions in combustion chambers for propulsion systems. RTO/NATO (Research and technology organisation) AGARDograph, AG-AVT-039, 2006.
[2] S. Candel, D. Durox, S. Ducruix, A.-L. Birbaud, N. Noiray, T. Schuller, Flame dynamics and combustion noise: progress and challenges, Int. J. Aeroacoust. 8 (2009) 1–56.
[3] G. Staffelbach, L.Y.M. Gicquel, G. Boudier, T. Poinsot, Large Eddy Simulation of self excited azimuthal modes in annular combustors, Proc. Combust. Inst. 32 (2) (2009) 2909–2916.
[4] C. Sensiau, F. Nicoud, T. Poinsot, A tool to study azimuthal standing and spinning modes in annular combustors, Int. J. Aeroacoust. 8 (2009) 57–67.
[5] M. Hauser, M. Lorenz, T. Sattelmayer, Influence of transversal acoustic excitation of the burner approach flow on the flame structure, GT2010-22965, ASME, 2010.
[6] J. O'Connor, T. Lieuwen, Disturbance field characteristics of a transversely excited burner, Combust. Sci. Technol. 183 (5) (2011) 427–443.
[7] J. O'Connor, T. Lieuwen, M. Kolb, Visualization of shear layer dynamics in a transversely excited, annular premixing nozzle, in: 49th AIAA Aerospace Sci. Meet., 2011.
[8] T. Lieuwen, V. Yang, Combustion instabilities in gas turbine engines: Operational experience, fundamental mechanisms and modeling, AIAA, AG-AVT-039, 2005.
[9] F. Lespinasse, F. Baillot, E. Domingues, Responses of laminar premixed flames to a high frequency transverse acoustic field, in: 5th Eur. Combust. Meet., Cardiff, UK, 28th June–1st July 2011.
[10] F. Baillot, J.-B. Blaisot, G. Boisdron, C. Dumouchel, On the behavior of an air-assisted jet submitted to a transverse high-frequency acoustic field, J. Fluid Mech. 640 (2009) 305–342.
[11] S. Shanbhogue, D.-H. Shin, S. Hemchandra, D. Plaks, Tim Lieuwen, Flame sheet dynamics of bluff-body stabilized flames during longitudinal acoustic forcing, Proc. Combust. Inst. 32 (2009) 1787–1794.
[12] D. Durox, T. Schuller, S. Candel, Combustion dynamics of inverted conical flames, Proc. Combust. Inst. 30 (2005) 1717–1724.